American Mineralogist, Volume 83, pages 799–810, 1998

Distribution of cations and vacancies and the structure of defects in oxidized intermediate olivine by atomic-resolution TEM and image simulation

DAWN E. JANNEY* AND JILLIAN F. BANFIELD†

Department of Geology and Geophysics, University of Wisconsin–Madison, Madison, Wisconsin 53706-1692, U.S.A.

ABSTRACT

The Fe, Mg, and vacancy distributions in oxidized olivine of intermediate composition and the crystal structures of associated planar defects were examined by a combination of atomic-resolution transmission electron microscopy, image analysis, and image simulation. Simulated images using various structures and site occupancies show that the defects are not laihunite-like layers within an essentially normal olivine, but instead are integral parts of a highly oxidized crystal with a high degree of cation and vacancy ordering and a distorted olivine structure. A possible new structure was derived as a variant of previously published refinements for oxidized fayalite (laihunite-3*M*), with one defect row per unit cell instead of two. Details in high-resolution images are extremely sensitive to variations in atomic positions and site occupancies. Semiquantitative constraints on relative magnitudes of electron densities provided by image simulation were combined with crystal chemical constraints based on local charge balance and compositional constraints from analytical electron microscopy in a series of linear equations, which were solved to provide several candidate models for the distribution of Fe, Mg, and vacancies. Simulations using the new structure and an occupancy model in which essentially all of the Fe is Fe^{3+} in M2 sites and all of the vacancies are in M1 sites match significant characteristics of HRTEM images obtained at Scherzer defocus and at overfocused conditions. This ordering scheme is similar to that of true laihunites and may result from differences in site and cation sizes.

INTRODUCTION

Numerous papers have addressed site occupancies and ordering of divalent octahedral cations in olivines. Recent examples include Redfern et al. (1997) for FeMn and MgMn olivines, Chakraborty (1997) for FeMg olivines, Müller-Sommer et al. (1997) for CoMg olivines, and Chen et al. (1996) for NiMg olivines. In contrast, little is known about the structural modifications required to accommodate significant quantities of trivalent octahedral cations. Laihunite, an intermediate-temperature oxidation product of fayalite (Kitamura et al. 1984; Kondoh et al. 1985) is the best-known example of a mineral displaying these modifications. Published laihunite compositions vary, but follow the general formula $\square_x Fe^{2+}_{2-3x} Fe^{3+}_{2x} SiO_4$ (Kondoh et al. 1985), where $\square$ represents vacancies and x ranges from 0.24 to 0.5 (Kondoh et al. 1985; Schaefer 1985; Kan and Coey 1985; Kitamura et al. 1984; Tamada et al. 1983; Shen et al. 1986).

Naturally occurring laihunites have been identified in igneous and metamorphic rocks from various locations (summarized by Schaefer 1985). Laihunite-like materials also have been produced synthetically by oxidizing FeMg, FeCo, FeMn, and FeCa olivines (Khisina et al. 1995, 1996; Iishi et al. 1989a, 1989b), but have not been studied in detail.

Laihunite has a distorted olivine structure (monoclinic, $\alpha = 91°$ in the unconventional space group $P2_1/b$ with unique a axis) (Tamada et al. 1983; Shen et al. 1986). One-layer, two-layer, and three-layer polytypes (where a "layer" corresponds to a distorted olivine unit cell) have been identified (references in Kondoh et al. 1985). X-ray refinements of the average structure (Tamada et al. 1983) and three-layer polytype (laihunite-3*M*; Shen et al. 1986) show a strongly layered structure in which the M1 sites are occupied by Fe^{2+} and vacancies in alternate layers parallel to (001), while the M2 sites are predominantly occupied by Fe^{3+}.

Banfield et al. (1990) interpreted periodic and nonperiodic planar crystallographic defects in oxidized olivine phenocrysts from basaltic andesites from the Abert Rim (south-central Oregon) as intergrowths of olivine and a naturally occurring Mg-rich, laihunite-like material. The defect-bearing areas are one of three distinct alteration assemblages in the phenocrysts: a magnetite-silica assemblage inferred to represent high-temperature oxidation of the olivine; the defect-bearing areas, which were inferred to represent intermediate-temperature (400–800 °C) oxidation; and a low-temperature assemblage formed by hydrothermal alteration and weathering (Banfield et al.

* Present address: Department of Geology, Arizona State University, P.O. Box 871404, Tempe, Arizona 85287, U.S.A. E-mail: djanney@asu.edu

† Present address: Mineralogical Institute, University of Tokyo, Hongo, Bunkyo-ku, Tokyo 113, Japan

0003–004X/98/0708–0799$05.00

1990). The planar defects occur in small patches, predominantly at edges of grains (Banfield et al. 1990). Defect spacing and composition both vary on a scale of a few hundred nanometers (Banfield et al. 1990).

The present study examines the crystal structures and site occupancies of periodic planar defects in the sample studied by Banfield et al. (1990). Because of the small spatial scale of these phenomena and the need to correlate chemical and microstructural observations, it was necessary to use transmission electron microscopy (TEM) techniques.

Experimental methods

The specimen in this study is an altered olivine phenocryst from a basaltic andesite lava flow that outcrops near Lake Abert (Abert Rim) in south–central Oregon. The specimen was previously examined by Banfield et al. (1990), who describe its geological context in detail.

AEM analyses of areas with planar defects showed metal cation (Fe+Mg) totals as low as 1.87 per four O atoms, while defect-free regions showed the 2 cations characteristic of stoichiometric olivine (Banfield et al. 1990). The AEM analyses also showed that the spacings of the planar defects increase with increasing magnesium content in the olivine over compositions ranging from approximately Fo 35 to Fo 85 (Banfield et al. 1990). Periodic planar defects in bulk compositions with Mg/(Mg+Fe) = 0.5 have spacings corresponding to every third olivine unit cell (Banfield et al. 1990) (approximately every 17–18 nm, based on Fo 50 and laihunite lattice parameters; Ghose et al. 1976; Shen et al. 1986).

Thin foils were prepared for electron microscopy by ion milling 30 μm thick olivine slices from petrographic thin sections and applying a light carbon coat (Banfield et al. 1990). Atomic-resolution transmission electron microscope images with the beam parallel to [100] were collected by David J. Smith at the Center for High Resolution Electron Microscopy (Arizona State University), using a JEOL 4000EX operated at 400 kV, with a range of thickness and defocus conditions. Thin regions in which periodic defects occurred every third unit cell were selected from two images recorded under very different defocus conditions for detailed comparison to simulated images.

Image simulations used the multislice algorithm as implemented in the EMS program (Stadelmann 1991). They used a C_s of 1.0 mm and other parameters appropriate for the microscope. Slice thickness was 1 unit cell (~0.48 nm in the direction parallel to the beam). Through-thickness and through-focus simulation series using thicknesses between 1 and 29 nm and defocus conditions between 124 nm underfocus and 196 nm overfocus established that the images represented ~49 nm underfocus (approximately Scherzer defocus) in an area ~6.7 nm (14 unit cells) thick and ~66 nm overfocus in an area ~15 nm (31 unit cells) thick. Fresnel fringes in the images are consistent with these conclusions.

Because the structure of the periodic defects was unknown, three candidate models specifying atomic positions were evaluated. Two of the models were based on suggestions in the literature; one was newly constructed for this paper. Extensive preliminary image simulations led to identification of relationships between site occupancies and characteristics of simulated images, and eventually to definition of a final series of 25 models that could be used to constrain site occupancies for the new structure. Each of these models satisfies local charge balance and has Mg/(Fe+Mg) = 0.5. All of the models in the final series were simulated using both the new structure model and normal Fo 50 olivine atomic positions (Ghose et al. 1976).

Constant isotropic thermal coefficients of 0.0045 nm^2 for Mg, 0.005 nm^2 for Fe, 0.003 nm^2 for Si, and 0.004 nm^2 for O were used in all of the simulations. These values are consistent with several published olivine structure analyses with R values <3% (e.g., Ghose et al. 1976; Fujino et al. 1981). Image simulations of Fo 50 olivine using the constant coefficients given above and published coefficients (Ghose et al. 1976) are indistinguishable.

Observations of high-resolution TEM images

Examination of several high-resolution TEM images viewed from the [100] (olivine and laihunite) direction (e.g., Fig. 1) showed that the planar defects were sharply bounded, that their apparent widths did not increase in slightly thicker areas of the specimen, and that there were no moiré fringes such as would be produced by an inclined boundary separating two slightly different crystal structures. These characteristics indicate that the defects are edge-on when viewed from this direction. Indexing calculated diffraction patterns from these images as olivine confirms that the defects are invariably parallel to (001). [Throughout this paper, olivine is assigned to the orthorhombic space group *Pbnm* and laihunite is assigned to the unconventional monoclinic space group $P2_1/b$ with the a axis unique. These space groups are habitually used in structure refinements of these minerals (e.g., Ghose et al. 1976; Shen et al. 1986), and describe comparable orientations of the olivine lattice.]

Defect spacing is variable, although it may be fairly constant over regions of at least several tens of nanometers. Defects spaced every second or third unit cell are common, but spacings of up to a micrometer occur in some areas. Defect periodicities involving fractions of olivine unit cells (e.g., every 2 ½ unit cells) were not observed. The appearance of the defects, and of the material between them, does not change recognizably with differences in defect spacing.

In images taken at Scherzer defocus conditions and specimen thickness of ~6.7 nm (Fig. 2a), the dominant feature is light colored, highly convoluted curves parallel to c. The defects are brighter areas in each curve, aligned to form rows perpendicular to the curves. There is no observable change in the shapes of the curves associated with the defects. Images taken at ~66 nm overfocus and ~15 nm specimen thickness (Fig. 2b) show closely

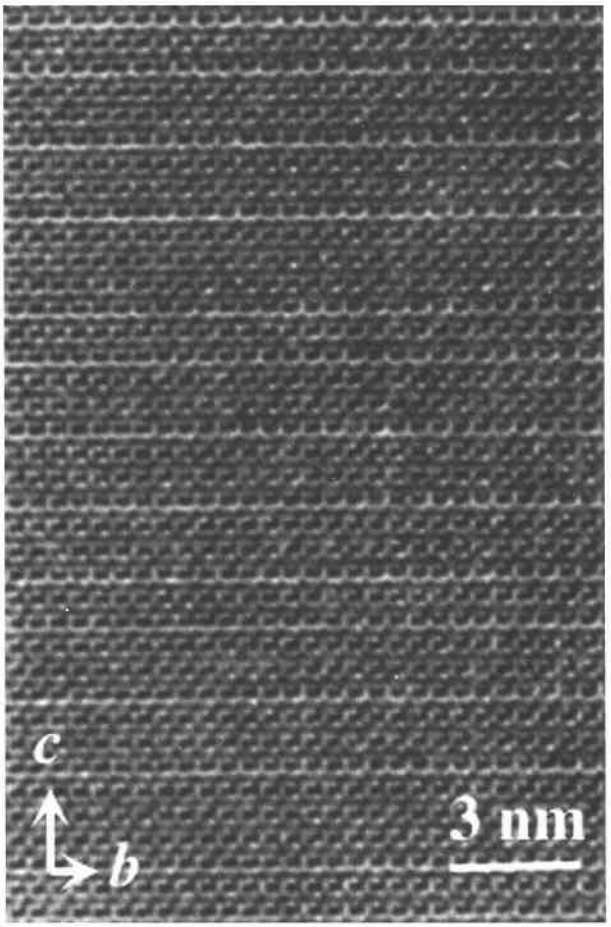

FIGURE 1. High-resolution TEM image of defects with nonperiodic two-, three-, and four-layer spacing. The appearance of the defects and the material between them is independent of defect spacing. Approximately Scherzer defocus (49 nm underfocus), thickness slightly greater than 6.7 nm, beam parallel to [100].

spaced individual bright spots. The defects appear as an unusually bright row of spots perpendicular to c with a dim row immediately above, but do not cause observable changes in the positions of the spots. These observations are consistent with changes in occupancy and small lattice distortions in an olivine-type structure. They preclude any interpretation of the defects as intergrowths of olivine and a mineral with a significantly different structure or lattice parameters, such as a humite-group mineral.

IMAGE-SIMULATION EVALUATION OF MODELS BASED ON THE LITERATURE

Two initial models for the defect structure of oxidized olivine were tested by comparing between image simulations and the high-resolution TEM images: interstratifications of laihunite in normal olivine and laihunite-3*M* with Mg^{2+} replacing Fe^{2+}.

Lattice parameters for both models are in Table 1. Unit-cell dimensions in the laihunite portions of the models are about 1% smaller than those in conventional laihunites (Shen et al. 1986; Tamada et al. 1983). This reduction is analogous to that in FeMg olivines, where lattice parameters of $Fo_{50}Fa_{50}$ (Ghose et al. 1976) are about 99% of those of fayalite (Fujino et al. 1981). The simulated images are not sensitive to small variations in unit-cell sizes and shapes.

Image simulation results are shown in Figure 3. Site occupancies and atomic positions are in Tables 2 and 3. Both models share a common olivine structure, with some distortions in laihunite portions. The triangles in the lower left corner of each image represent the positions of silica tetrahedra in one unit cell, projected onto (100). M1 octahedral sites are between the sides of triangles in adjacent horizontal rows, and M2 octahedral sites are between the base of one triangle and the apex of the adjacent triangle in the same row.

INTERSTRATIFIED OLIVINE AND AVERAGE MG-LAIHUNITE

Several researchers (Banfield et al. 1990, 1992; Khisina et al. 1995) have suggested that the defects in oxidized olivine are intergrowths of a laihunite-like mineral with normal olivine. The amount of magnesium in the laihunite-like mineral is not well constrained (Banfield et al. 1990, 1992), although Mössbauer spectroscopy suggests that it contains no Fe^{2+} (Khisina et al. 1995).

Figure 3 shows simulated images of a model consisting of one layer of average laihunite (Tamada et al. 1983), in which Mg^{2+} has been substituted for Fe^{2+}, sandwiched between two layers of fully disordered Fo 42.9. The overall composition is $\square_{0.40}Fe^{3+}_{0.80}Fe^{2+}_{2.00}Mg^{2+}_{2.80}Si_3O_{12}$ with an Mg/(Mg+Fe) ratio of 0.5. Atomic positions in the olivine portion are from the F_{50} F_{50} structure refinement by Ghose et al. (1986). The olivine and laihunite are joined along their mutual (001) planes at $z \sim \frac{1}{3}$ and $\sim \frac{2}{3}$. Slight mismatches in the a and b lattice parameters of the olivine and laihunite are ignored, as is the small deviation from orthorhombic symmetry produced by the monoclinic laihunite.

The simulated images (Figs. 3a and 3b) do not match the observed images (Fig. 2) in several important respects. The light curves in Figure 3a are offset across the defects, while those in Figure 2a are not, and the defects themselves are too bright. The asymmetrical spots adjacent to the defects in Figure 3b are similar to those in Figure 2b, but the columnar arrangement of the spots between the defects is not.

Simulated images from a closely related model in which a layer of true (Fe-) laihunite is sandwiched between two layers of normal Fo 80 olivine are quite similar to Figures 3a and 3b. These do not match the observed images for the same reasons.

MG-LAIHUNITE 3*M*

The Mg-laihunite 3*M* model is based on an X-ray structure refinement of an (Fe-) laihunite 3*M* with a composition of $\sim\square_{0.40}Fe^{2+}_{0.80}Fe^{3+}_{0.80}SiO_4$ (Shen et al. 1986). Mg^{2+}

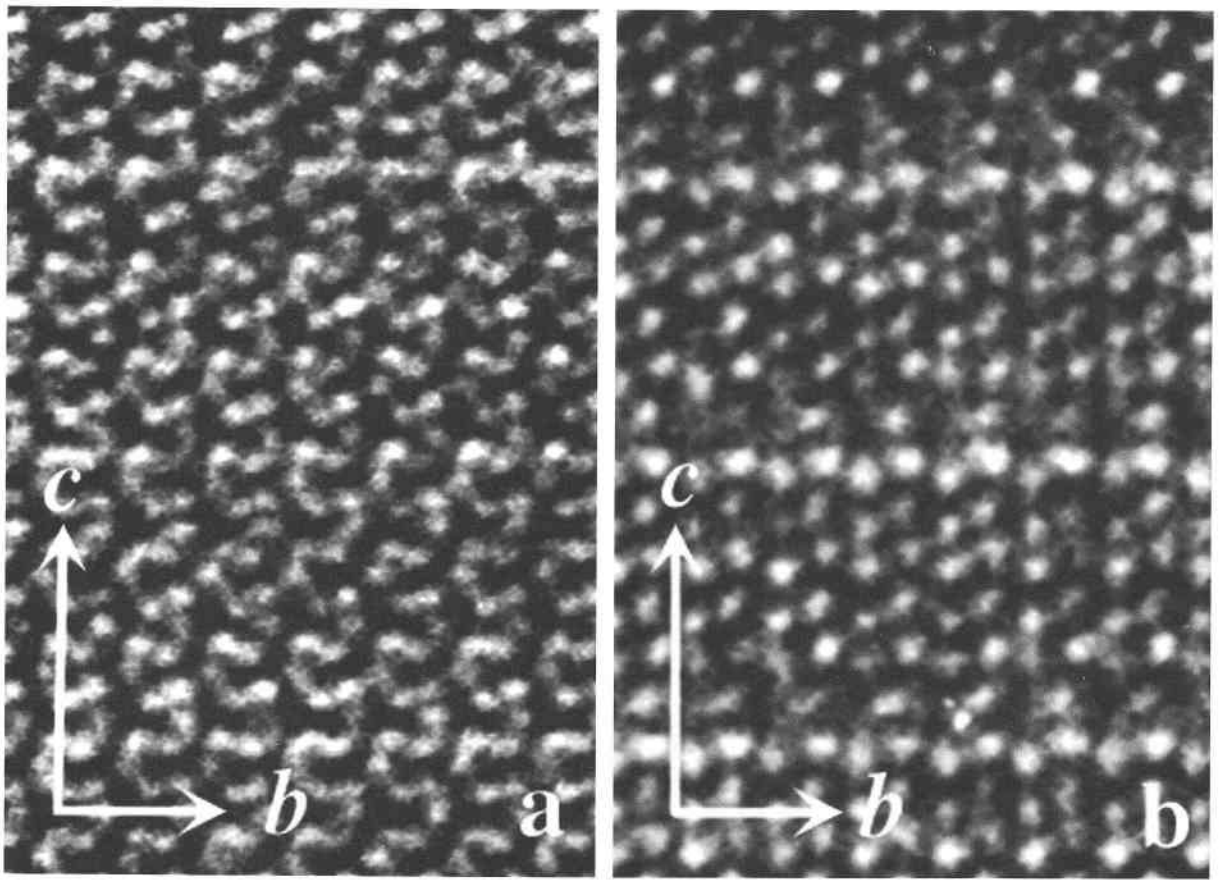

FIGURE 2. High-resolution TEM images of defects with three-layer spacing, beam parallel to [100]. Defects are primarily changes in image brightness rather than distortions of the basic pattern. Arrows show crystallographic orientation and size of one unit cell (~1.0 × 1.8 nm). (**a**) ~Scherzer defocus, ~6.7 nm specimen thickness. (**b**) ~66 nm overfocus, ~15.0 nm specimen thickness.

was substituted for Fe^{2+} throughout, producing a bulk composition of $\square_{0.40}Fe^{3+}_{0.80}Mg^{2+}_{0.80}SiO_4$.

Simulated images from the Mg-laihunite 3*M* model (Figs. 3c and 3d) again show significant differences from the observed images. The model has paired rows of defects one olivine unit cell apart; this spacing was never observed in the oxidized olivine in this study. The light curves in Figure 3c stair-step diagonally rather than being parallel to *c*, and the defects are even brighter relative to the rest of the image than they are in Figure 3a. The positions of the spots in Figure 3d are a slight improvement over the olivine portions of Figure 3b, but are still not correct.

TABLE 1. Lattice parameters

Structure model	Space group	*a* (Å)	*b* (Å)	*c* (Å)	α °
Fo_{50} Fa_{50}	*Pbnm*	4.794	10.339	18.125	90
Interstratified olivine, laihunite	*P*2$_1$/*b**	4.794	10.339	17.840	90
Mg-laihunite 3*M*	*P*2$_1$/*b**	4.825	10.053	17.272	91
Single-defect-row structure	*P*2$_1$/*b**	4.825	10.053	17.185	91

Note: For all models, β and γ = 90 °.
* *a* unique.

DEVELOPMENT OF A NEW STRUCTURE MODEL WITH A SINGLE DEFECT ROW

The structure model for Mg-laihunite 3*M* discussed above has two closely spaced rows of vacancies per unit cell, while observations of the defects in oxidized intermediate olivine indicate that there should be only one. Consequently a new structure model was developed by removing one defect row in Mg-laihunite 3*M* (Table 3).

Octahedral and tetrahedral cation positions in the new model were developed by analyzing displacements in Mg-laihunite 3*M* relative to olivine, then propagating displacements from the areas outside the paired defects symmetrically around the single defect row in the new structure. O atom positions were generated from tetrahedral distortions and rotations relative to olivine. The origin of the unit cell was shifted to position the defect row in the center. Figure 4 shows the resulting cation positions and tetrahedral distortions and rotations relative to those in olivine. The maximum displacements relative to Fo 50 atomic positions are ~0.11 Å for any tetrahedral

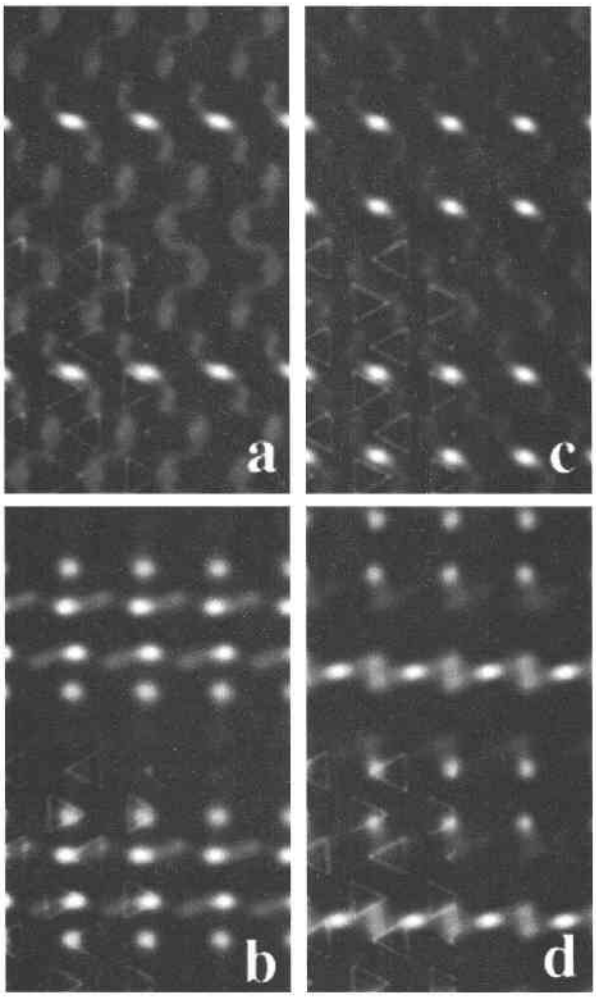

FIGURE 3. Image-simulation evaluation of models based on the literature. Each image shows four unit cells. Triangles (lower left unit cell for each image) indicate projected positions of silica tetrahedra determined from the corresponding electron potential map. Top row: Scherzer defocus and ~6.7 nm specimen thickness. Bottom row: ~66 nm overfocus and ~15.0 nm specimen thickness. (**a** and **b**) Normal Fo 42.9 olivine (top and bottom thirds of each unit cell) interstratified with average Mg-laihunite (middle third). (**c** and **d**) Mg-laihunite 3*M*.

cation, ~0.15 for any octahedral cation, and ~0.23 for any O atom [~0.09, ~0.15, and ~0.16 Å parallel to the (100) plane].

DEVELOPMENT OF SITE-OCCUPANCY MODELS

To study possible site occupancies for the new model, we specified a system of linear equations whose solutions are site occupancies that have a defect every third row, produce an overall Mg/(Fe+Mg) ratio of 0.5, and are locally charge balanced. Seven equations were used: two specifying M2 site occupancies, two specifying electron densities in M1 sites, two specifying local charge-balance relationships, and one specifying bulk composition. Different site occupancy models for image-simulation evaluation were produced by changing the oxidation state of the Fe and the distribution of the Fe, Mg, and vacancies between the sites.

TABLE 2. Octahedral site occupancies for models from the literature

z-coordinate	Site type	Interstratified olivine and laihunite			Mg-laihunite 3*M*		
		Mg^{2+}	Fe	□	Mg^{2+}	Fe^{3+}	□
~0.00	M1	0.429	0.571	—	1.0	—	—
~0.08	M2	0.429	0.571	—	0.2	0.8	—
~0.16	M1	0.429	0.571	—	—	—	1.0
~0.25	M2	0.429	0.571	—	0.2	0.8	—
~0.33	M1	1.0	—	—	1.0	—	—
~0.41	M2	0.2	0.8	—	0.2	0.8	—
~0.50	M1	0.2	—	0.8	—	—	1.0
~0.58	M2	0.2	0.8	—	0.2	0.8	—
~0.67	M1	1.0	—	—	1.0	—	—
~0.75	M2	0.429	0.571	—	0.2	0.8	—
~0.83	M1	0.429	0.571	—	0.67	—	0.33
~0.91	M2	0.429	0.571	—	0.2	0.8	—

Note: Origin of Mg-laihunite 3*M* unit cell translated by $z = -1/3$ for compatibility with interstratified olivine-laihunite and single-defect-row structures.

Figure 5 illustrates designations for site occupancies in the equations. Adjacent M1 and M2 sites with similar heights can be regarded as lying along zigzags parallel to *c*. M1 sites are considered to be either "a" sites, which lie in the defects, or "c" sites, which lie between them. M2 sites are considered to be either "b" sites, which are adjacent to the defects, or "d" sites, which are between them. Site occupancies are designated by a letter indicating the site type ("a", "b", "c", or "d") and a subscript (1 for Mg and 2 for Fe).

The site-occupancy model makes five assumptions: (1) all tetrahedral sites are occupied by Si; (2) all anion sites are occupied by O; (3) the defects involve only one row

TABLE 3. Atomic positions for constructed models

Site type	Interstratified olivine, laihunite			Single-defect-row structure		
	x	*y*	*z*	*x*	*y*	*z*
M1	0	0	0	0	0	0
M1	0	0	0.167	0	0	0.166
M1	0	0	0.333	0.999	0.991	0.339
M1	0	0	½	0	0	½
M2	0.987	0.721	0.083	0.005	0.725	0.083
M2	0.487	0.779	0.250	0.504	0.778	0.249
M2	0.505	0.226	0.419	0.509	0.234	0.418
T	0.072	0.404	0.083	0.059	0.404	0.083
T	0.572	0.096	0.250	0.559	0.100	0.249
T	0.060	0.404	0.416	0.059	0.412	0.416
O	0.217	0.336	0.012	0.220	0.328	0.009
O	0.734	0.408	0.083	0.723	0.398	0.080
O	0.214	0.550	0.083	0.174	0.555	0.084
O	0.217	0.336	0.155	0.201	0.329	0.154
O	0.717	0.164	0.178	0.701	0.175	0.178
O	0.714	0.950	0.250	0.674	0.949	0.248
O	0.234	0.092	0.250	0.223	0.107	0.252
O	0.717	0.165	0.322	0.72	0.176	0.323
O	0.217	0.327	0.344	0.222	0.335	0.346
O	0.724	0.395	0.415	0.727	0.401	0.413
O	0.327	0.054	0.419	0.328	0.060	0.418
O	0.196	0.323	0.489	0.199	0.326	0.486

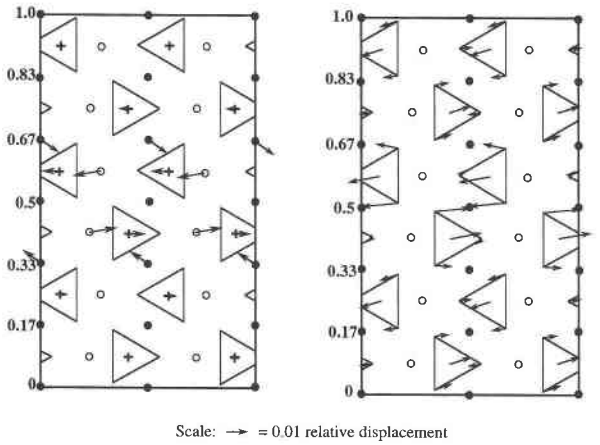

FIGURE 4. Atomic displacements in the single-defect-row structure, projected onto (100) plane. Filled circles = M1 sites. Open circles = M2 sites. Crosses = Tetrahedral sites (Si). (**left**) Cation displacements relative to olivine. Only displacements ≥0.0015 are shown. (**right**) Tetrahedral distortions and rotations relative to olivine.

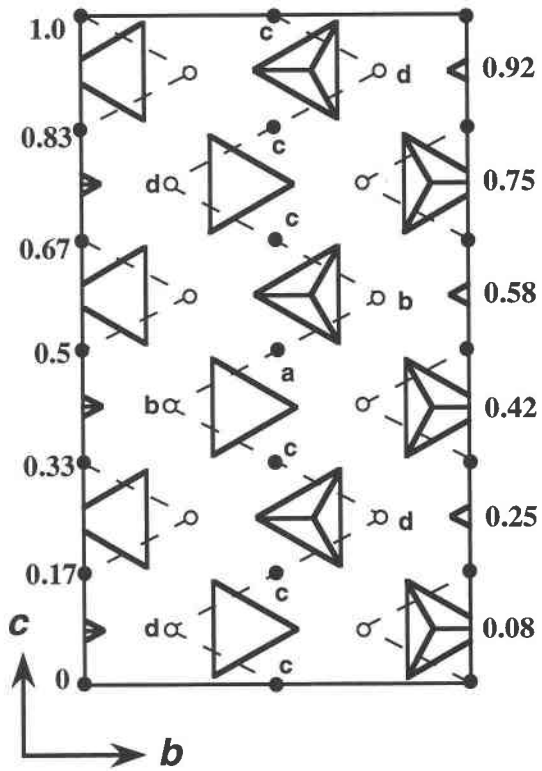

FIGURE 5. Schematic three-layer olivine structure projected onto the (100) plane to illustrate site nomenclature used in linear equations. Filled circles = M1 sites; z-coordinates at left. Open circles = M2 sites; z-coordinates at right. Dashed zigzags connect M1 and M2 sites at the same height (x-coordinate). Small letters "a" through "d" designate sites for linear equations.

of M1 sites and the adjacent M2 sites; (4) the ordering behavior of Fe^{2+} and Fe^{3+} is similar; and (5) there is no Fe in the "a" sites (i.e., $a_2 = 0$), which form the defect row. The first two assumptions are required for consistency with both normal olivine (e.g., Ghose et al. 1976) and laihunite (Shen et al. 1986; Tamada et al. 1983). The third assumption is supported by the appearance of the defects in observed images (Figs. 1 and 2), and is consistent with the rapid decrease in lattice distortions relative to olivine in the single-defect-row structure (Fig. 4). The fourth and fifth assumptions are supported by image simulation results and will be discussed below.

Careful consideration of the Scherzer-defocus images in the top row of Figure 3 suggests that the position of the light-colored vertical curves relative to the tetrahedra is sensitive to M1 site occupancy. The curves invariably pass through the positions of M1 sites with vacancies, and avoid the positions of fully occupied M1 sites. Thus, the curves in the interstratified olivine and laihunite model (Fig. 3a) avoid the M1 positions in the olivine sections of the model (which has no M1 vacancies), then are offset to pass through the vacant M1 site in the laihunite portion of the model. The diagonal stair-steps in the Mg-laihunite 3*M* model (Fig. 3c) occur because the curves alternately pass through and avoid vacant and fully occupied M1 sites.

M1 site occupancy also controls the relative brightness of the defects: they are slightly brighter relative to the rest of the curves in the Mg-laihunite 3*M* model, where the M1 sites in the defects are fully vacant, than in the interstratified olivine-laihunite model, where they are occupied by 0.2 Mg atoms.

Preliminary simulations showed that the total electron density (ed) of the atoms in the "a" and "c" sites is crucial in understanding characteristics of the simulated images. Thus, Equations 1 and 2 (below) specify a_{ed} and c_{ed}, the electron densities of the atoms occupying the "a" and "c" sites, respectively, as a multiple of the electron density of one Mg atom.

$$a_{ed} = a_1 \quad (1)$$

$$c_{ed} = c_1 + 2c_2. \quad (2)$$

The "$c_1 + 2c_2$" term in Equation 2 indicates that Mg can be exchanged for Fe at a 2:1 ratio without changing the appearance of the simulated images. This exchange rate reflects the ratio of the electron scattering factor for Mg to that of Fe (Doyle and Turner 1968) for values of $(\sin\theta)/\lambda$ between 0.2 and 0.5. The ratio of the scattering factors for Mg : Fe lies between about 1.82 and 2.08 over this angular range, with an average value very close to 2.0, and is essentially independent of the oxidation state of the Fe. If it were not assumed that there is only Mg in "a" sites, there would be a similar exchange ratio in Equation 1.

The preliminary image simulations were insensitive to differences in the electron densities of Fe and Mg occupying the M2 ("b" and "d") sites. Consequently, Equations 3 and 4 (which specify the "b" site occupancy, b_{occ},

TABLE 4a. Site occupancies for final simulations with 100% Fe^{3+}

a_{ed}	0.45*	0.45	0.45	0.45†	0.55	0.45	0.45	0.45	0.45‡	0.55
b_{occ}	1*	0.95	1	1†	1	0.95	1	1	1‡	1
c_{ed}	0.65*	0.75	0.75	0.75†	0.75	0.85	0.85	0.85	0.85‡	0.85
d_{occ}	1*	1	0.85	1†	1	1	0.79	0.90	1‡	1
a_1	0.45	0.45	0.45	0.45	0.55	0.45	0.45	0.45	0.45	0.55
b_1	0.09	0	0.20	0.14	0.23	0.05	0.27	0.23	0.19	0.28
b_2	0.91	0.95	0.80	0.86	0.77	0.90	0.73	0.77	0.81	0.72
c_1	0.61	0.55	0.75	0.51	0.47	0.45	0.75	0.57	0.41	0.37
c_2	0.02	0.10	0	0.12	0.14	0.20	0.05	0.14	0.22	0.24
d_1	0.28	0.40	0.05	0.38	0.36	0.50	0.02	0.26	0.48	0.46
d_2	0.72	0.60	0.80	0.62	0.64	0.50	0.77	0.64	0.52	0.54

Note: $Charge_{Fe} = 3.0$, $Mg_{tot} = Fe_{tot} = 4.8$. Composition $\sim\square_{0.40}Fe^{3+}_{0.80}Mg^{2+}_{0.80}SiO_{4+}$
* Figure 7 a, b, g, h; Figure 8.
† Figure 7 c, d, i, j.
‡ Figure 7 e, f, k, l.

and the "d" site occupancy, d_{occ}, respectively) are expressed in terms of the total number of atoms in each site, and allow Mg to be exchanged for Fe at a 1:1 ratio.

$$b_{occ} = b_1 + b_2 \quad (3)$$

$$d_{occ} = d_1 + d_2. \quad (4)$$

Equations 5 and 6 are an expression of local charge balance within an olivine-like structure. More specifically, the equations were defined by noting that the average charge for all octahedral sites is +2 in olivine, and requiring that any difference from this average charge resulting from the introduction of a vacancy or +3 cation into one octahedral site must be compensated by corresponding changes in adjacent octahedral sites. Derivations for the charge-balance equations are in Appendix 1.

$$2c_1 + charge_{Fe} \times c_2 + 2d_1 + charge_{Fe} \times d_2 = 4 \quad (5)$$

$$2a_1 + 4b_1 + 2 \times b_2 \times charge_{Fe} + 2c_1 + c_2 \times charge_{Fe} = 8. \quad (6)$$

In these equations, $charge_{Fe}$ is the average charge of an Fe ion (for example, $charge_{Fe} = 2.9$ if 90% of the Fe is Fe^{3+} and 10% is Fe^{2+}).

Equations 7 and 8 express the bulk composition in terms of Mg_{tot} and Fe_{tot} (the total magnesium and iron per zigzag in one unit cell of oxidized olivine, respectively).

$$Mg_{tot} = a_1 + 2b_1 + 5c_1 + 4d_1 \quad (7)$$

$$Fe_{tot} = 2b_2 + 5c_2 + 4d_2. \quad (8)$$

It is sufficient to specify either Fe_{tot} or Mg_{tot} in the final system of linear equations; the other one follows automatically as a consequence of the charge-balance and site-occupancy constraints.

IMAGE-SIMULATION RESULTS FOR THE NEW MODELS

Table 4 specifies a final series of image simulations, which use site occupancies that satisfy Equations 1 to 7. Values of c_{ed} range from 0.65 (possible only if essentially all Fe is Fe^{3+} in M2 sites and all vacancies are in M1 sites) to 0.85 (higher than the value at which preliminary simulations showed that the white curves in Scherzer images no longer passed through M1 positions). Preliminary simulations showed that a value of 0.45 for a_{ed} produced the correct defect brightness for c_{ed} between 0.65 and 1.0; however, a few simulations with $a_{ed} = 0.55$ were also included in the final group. The fraction of Fe that is Fe^{3+} ranges from 100% ($charge_{Fe} = 3$) to 70% ($charge_{Fe} = 2.7$); lower percentages have so few vacancies that they are inconsistent with the possible ranges for a_{ed} and c_{ed}. Possible values of b_{occ} and d_{occ} vary from model to model, depending on a_{ed}, c_{ed}, and the fraction of Fe^{3+}, but are simulated at intervals throughout their ranges.

Site occupancies in each section (a to d) of Table 4 have different fractions of Fe^{3+}. As the Fe becomes less oxidized, ordering of Fe into M2 sites and Mg into M1 sites increases, and the total number of vacancies decreases. Ordering of Fe and Mg also increases if vacancies are introduced into M2 sites (b_{occ} or $d_{occ} < 1$). Blanks indicate cases where site occupancies meeting all of the con-

TABLE 4b. Site occupancies for final simulations with 90% Fe^{3+}

a_{ed}	0.45	0.45	0.45	0.45	0.55	0.45	0.45	0.45	0.45	0.55
b_{occ}	1	0.95	1	1	1	0.95	1	1	1	1
c_{ed}	0.67	0.75	0.75	0.75	0.75	0.85	0.85	0.85	0.85	0.85
d_{occ}	1	1	0.90	1	1	1	0.81	0.90	1	1
a_1	0.45	—	0.45	0.45	0.55	—	0.45	0.45	0.45	0.55
b_1	0.02	—	0.11	0.06	0.16	—	0.20	0.16	0.11	0.21
b_2	0.98	—	0.89	0.94	0.84	—	0.80	0.84	0.89	0.79
c_1	0.67	—	0.75	0.59	0.55	—	0.79	0.65	0.49	0.45
c_2	0	—	0	0.08	0.10	—	0.03	0.10	0.18	0.20
d_1	0.27	—	0.12	0.35	0.32	—	0.02	0.22	0.45	0.42
d_2	0.73	—	0.78	0.65	0.68	—	0.79	0.68	0.55	0.58

Note: $Charge_{Fe} = 2.9$, $Mg_{tot} = Fe_{tot} = 4.9$. Composition $\sim\square_{0.37}Fe^{3+}_{0.73}Fe^{2+}_{0.08}Mg^{2+}_{0.82}SiO_{4+}$

TABLE 4c. Site occupancies for final simulations with 80% Fe^{3+}

a_{ed}	0.45	0.45	0.45	0.45	0.55	0.45	0.45	0.45	0.45*	0.55†
b_{occ}	1	0.95	1	1	1	0.95	1	1	1*	1†
c_{ed}	0.65	0.75	0.75	0.75	0.75	0.85	0.85	0.85	0.85*	0.85†
d_{occ}	1	1	0.85	1	1	1	0.83	0.90	1*	1†
a_1	—	—	—	—	0.55	—	0.45	0.45	0.45	0.55
b_1	—	—	—	—	0.08	—	0.12	0.08	0.02	0.13
b_2	—	—	—	—	0.92	—	0.88	0.92	0.98	0.87
c_1	—	—	—	—	0.63	—	0.84	0.73	0.57	0.53
c_2	—	—	—	—	0.06	—	0	0.06	0.14	0.16
d_1	—	—	—	—	0.29	—	0.02	0.19	0.42	0.39
d_2	—	—	—	—	0.72	—	0.81	0.72	0.59	0.62

Note: $Charge_{Fe} = 2.8$, $Mg_{tot} = Fe_{tot} = 5.0$. Composition $\sim\square_{0.33}Fe^{3+}_{0.67}Fe^{2+}_{0.17}Mg^{2+}_{0.83}SiO_{4+}$

* Figure 6 a to d.

† Figure 6 e to h.

straints expressed in the linear equations do not exist. Cross-references are given to simulation results in Figures 6 and 7.

Each set of occupancies in Table 4 was simulated using atomic positions from both normal Fo 50 olivine (Ghose et al. 1976) and the new single-defect-row model. These structures represent extremes of ordering and oxidation: normal Fo 50 is essentially disordered and has no Fe^{3+}, while the single-defect-row structure perpetuates lattice distortions from the highly oxidized, highly ordered laihunite-3*M* structure. It seems reasonable to expect that intermediate stages of ordering and oxidation would have intermediate lattice distortions.

Within each structure model, almost all of the variability in the simulated images can be explained by different values of a_{ed} and c_{ed}. Because of the assumption that there is no Fe in the "a" sites, a_{ed} directly reflects the amount of vacancy in these sites ($1 - a_{ed}$). Table 4 shows that the total number of atoms in each "c" site ($c_1 + c_2$) is almost constant for each combination of a_{ed}, b_{occ}, d_{occ}, and fraction of Fe^{3+}. Thus, differences in c_{ed} reflect the Fe:Mg ratio in the "c" sites rather than differences in the total number of atoms. These differences in turn correspond to different degrees of Fe:Mg ordering in the "b" and "d" sites.

Figure 6 shows typical simulations with different values of a_{ed}. Comparison of Figure 2a with the top row of Figure 6 shows that the defects have the appropriate brightness when $a_{ed} = 0.45$ ("a" sites have 0.55 vacancies), but are too dim when $a_{ed} = 0.55$ ("a" sites have only 0.45 vacancies). If Fe were allowed in the "a" sites, it would substitute for Mg using a 1:2 ratio in like that in Equation 2, requiring an even higher amount of vacancy in the "a" sites to produce the same defect brightness.

Figure 7 shows typical simulation results with different values of c_{ed}. All of the images have a total of 0.63 atoms per "c" site, and increases in c_{ed} are due entirely to decreasing Fe:Mg order. Scherzer-defocus images with $c_{ed} = 0.65$ display continuous white curves passing through all M1 positions (Figs. 7a and 7g). All of the vacancies are in M1 sites, and essentially all of the Fe is in M2 sites (Table 4a). With increasing Fe:Mg disorder, the curves become discontinuous or much less bright in the M1 positions outside the defects and change their shapes slightly (Figs. 7c, 7i, and 7k). Further increases in Fe:Mg disorder produce continuous curves that stair-step across the defects and avoid M1 sites between them (Fig. 7e and single-defect-model simulations with $c_{ed} = 1.0$, which are not shown), similar to those in interstratified olivine and laihunite (Fig. 3a). The overfocused simulations in the bottom row of Figure 7 are relatively insensitive to c_{ed}, although there are subtle changes in the shapes and intensities of some of the white spots in the single-defect-row model (compare Figs. 7h and 7j).

Despite the generally similar behavior of simulated images using the olivine and single-defect-row atomic coordinates, consistent differences between the two illustrate the sensitivity of the simulations to small changes in atomic positions. The white curves in Scherzer images

TABLE 4d. Site occupancies for final simulations with 70% Fe^{3+}

a_{ed}	0.45	0.45	0.45	0.45	0.55	0.45	0.45	0.45	0.45	0.55
b_{occ}	1	0.95	1	1	1	0.95	1	1	1	1
c_{ed}	0.65	0.75	0.75	0.75	0.79	0.85	0.85	0.85	0.85	0.85
d_{occ}	1	1	0.85	1	1	1	0.80	0.90	1	1
a_1	—	—	—	—	0.55	—	—	—	—	0.55
b_1	—	—	—	—	0	—	—	—	—	0.03
b_2	—	—	—	—	1	—	—	—	—	0.97
c_1	—	—	—	—	0.67	—	—	—	—	0.61
c_2	—	—	—	—	0.06	—	—	—	—	0.12
d_1	—	—	—	—	0.29	—	—	—	—	0.35
d_2	—	—	—	—	0.71	—	—	—	—	0.65

Note: $Charge_{Fe} = 2.7$, $Mg_{tot} = Fe_{tot} = 5.1$. Composition $\sim\square_{0.30}Fe^{3+}_{0.60}Fe^{2+}_{0.26}Mg^{2+}_{0.85}SiO_{4+}$

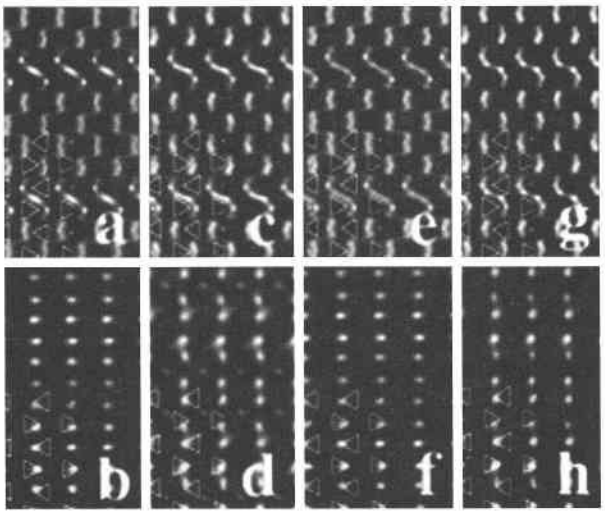

FIGURE 6. Typical simulations showing the effects of different values of a_{ed}. All images have b_{occ} = 1, c_{ed} = 0.85 (~0.30 vacancy), d_{occ} = 1, and 80% of Fe as Fe^{3+} (Table 4c). Top row: Scherzer defocus, ~6.7 nm thickness. Bottom row: ~66 nm overfocus, ~15 nm thickness. Triangles (lower left unit cell for each image) indicate projected positions of silica tetrahedra. (**a**) to (**d**) a_{ed} = 0.45. (**a**) and (**b**) olivine atomic coordinates. (**c**) and (**d**) single-defect-row structure. Defect brightness matches observed. (**e**) to (**h**) a_{ed} = 0.55. (**e**) and (**f**) olivine atomic coordinates. (**g**) and (**h**) single-defect-row structure. Defects in Scherzer images (top row) are not bright enough relative to the rest of the light-colored curves.

move out of the M1 positions with a lower value of c_{ed} using the olivine atomic coordinates than in the single-defect-row structure (Fig. 7). The overfocused simulations using olivine atomic coordinates show columns of white spots (Figs. 6b, 6f, 7b, 7d, and 7f), which appear identical in all of the simulations in Table 4. In contrast, the white spots in the overfocused single-defect-row simulations (Figs. 6d, 6h, 7h, 7j, and 7l) change intensity with variations in site occupancies.

Simulated images for the single-defect-row structure with a_{ed} = 0.45, b_{occ} = 1, c_{ed} = 0.65, d_{occ} = 1, and 100% of Fe as Fe^{3+} match the essential characteristics of the observed images of defects with 3-layer spacings at both Scherzer defocus and 66 nm overfocus conditions (Fig. 8), and thus can be considered a reasonable approximation to both the structure and site occupancies in the oxidized olivine. (Simulated images for the corresponding model with 90% Fe^{3+} are a slightly less good match.) This model represents fully oxidized olivine with a Mg/(Fe+Mg) ratio of 0.5 ($\square_{0.40}Mg^{2+}_{0.80}Fe^{3+}_{0.80}SiO_4$). The total number of vacancies is identical to that in the laihunite analyses used as the basis for the structure derivation (Tamada et al. 1983; Shen et al. 1986), and the iron-magnesium ratio corresponds to that previously determined by AEM measurements in areas of this specimen with 3-layer defect spacings (Banfield et al. 1990).

The observed and simulated images in Figure 8 do not match perfectly. Shapes of curves and dark regions in the Scherzer image (Fig. 8a) are somewhat different, as are positions of white spots in the overfocused images (Fig. 8b). Both of these characteristics are quite sensitive to small shifts in atomic positions (compare Fig. 6a with 6c, 6b with 6d, 6e with 6g, 6f with 6h, 7a with 7g, 7b with 7h, 7c with 7i, 7d with 7j, 7e with 7k, and 7f with 7l. Images in each pair have the same site occupancies; differences are entirely due to lattice distortions in the single-defect-row structure.) Thus, differences between the simulated and observed images in Figure 8b probably result from small differences in real and simulated atomic positions rather than from fundamental structural or site-occupancy characteristics. The apparent asymmetry around the defects in the observed overfocused images may also reflect a small amount of beam tilt (D.J. Smith, written communication).

Several possible sources of small errors exist in atomic positions in the single-defect-row structure. Size differences between Fe and Mg are not considered in the model except as they affect lattice parameters. The organizations of the defects in laihunite and Mg-laihunite also differ in ways other than the number of defect rows: laihunite has both fully vacant and fully occupied M1 sites, whereas Mg-laihunite has partial vacancies in all M1 sites. Thus, it is not surprising that atomic positions are not perfect in a model constructed by assuming that offsets in rows adjacent to the defects are the same in both structures. Because systematic criteria for making very small changes in atomic positions were absent, we did not attempt to improve the single-defect-row model by arbitrarily moving individual atoms.

Although differences exist between the observed and simulated images in Figure 8, consistent trends in the simulated images (e.g., Figs. 6 and 7) indicate that the oxidized olivine must have large amounts of vacancies in M1 sites (requiring high fractions of Fe^{3+}) and a high degree of ordering in which essentially all vacancies are in M1 sites and all iron is in M2 sites. These conclusions are the same for both the olivine and the single-defect-row structures, and thus are independent of the precise structure model used. Given these results, it seems highly unlikely that there is significant Fe in the defect rows (where it would require even larger amounts of vacancy to produce similar defect brightness in simulated images) or major differences in the ordering behavior of Fe^{2+} and Fe^{3+}.

DISCUSSION

X-ray structure refinements (Tamada et al. 1983; Shen et al. 1986), infrared spectroscopy, considerations of octahedral site and cation sizes (Schaefer 1985), and Mössbauer spectral analyses (Kan and Coey 1985) of Fe-laihunites agree that M2 sites are fully occupied, that all Fe^{3+} is in M2 sites, and that M1 sites contain a mixture of vacancies and Fe^{2+}. These observations are similar to the Mg-laihunite site occupancies presented here (except, of course, that Mg-laihunite has Mg^{2+} where true laihunites have Fe^{2+}).

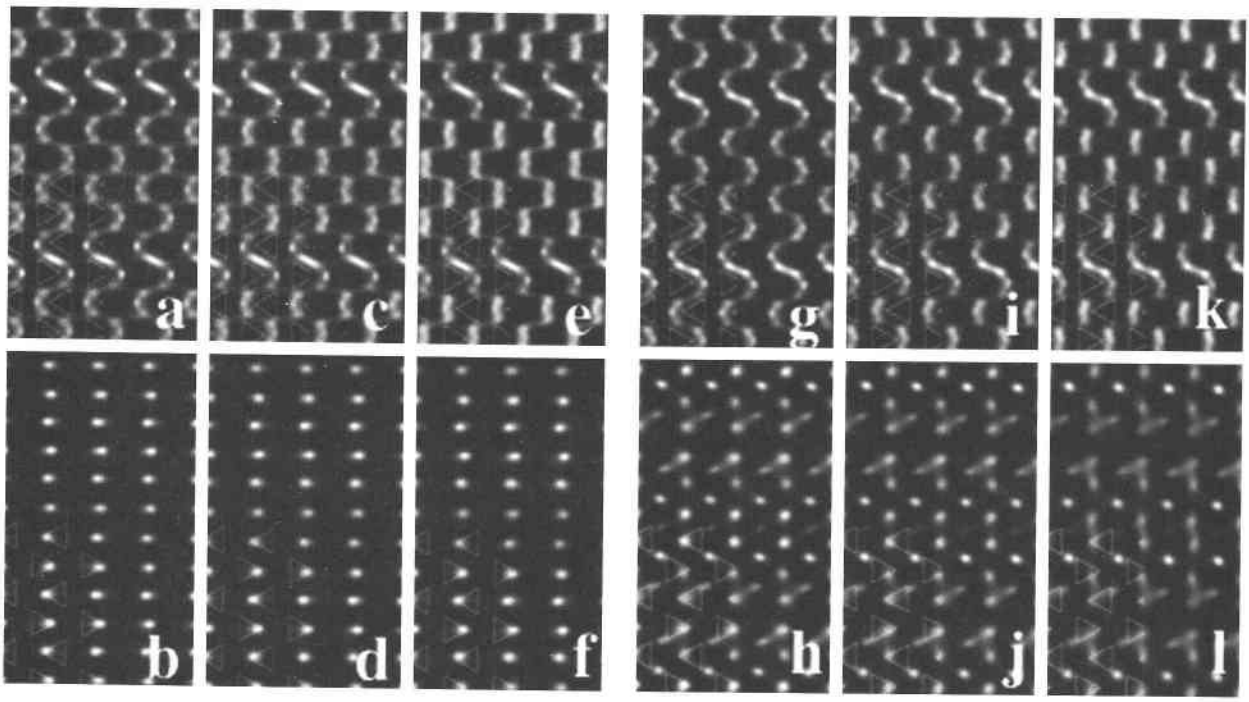

FIGURE 7. Typical simulations showing the effects of different values of c_{ed}. All images have $a_{ed} = 0.45$, $b_{occ} = 1$, $d_{occ} = 1.0$, 0.37 vacancy in each "c" site ($c_1 + c_2 = 0.63$), and 100% of Fe as Fe^{3+} (Table 4a). Top row: Scherzer defocus, ~6.7 nm thickness. Bottom row: ~66 nm overfocus, ~15 nm thickness. Triangles (lower left unit cell for each image) indicate projected positions of silica tetrahedra. (**a**) to (**f**) olivine atomic coordinates. (**a**) and (**b**) $c_{ed} = 0.65$. (**c**) and (**d**) $c_{ed} = 0.75$. (**e**) and (**f**) $c_{ed} = 0.85$. (**g** to **l**) single-defect-row structure. (**g**) and (**h**) $c_{ed} = 0.65$. (**i**) and (**j**) $c_{ed} = 0.75$. (**k**) and (**l**) $c_{ed} = 0.85$. Curves in Scherzer images (top row) are continuous and pass through M1 sites when $c_{ed} = 0.65$, become discontinuous or less bright in M1 sites when $c_{ed} = 0.75$, and avoid M1 sites when $c_{ed} = 0.85$.

The similar ordering behavior of Fe- and Mg-laihunites may reflect energetic differences between vacancies in the M1and M2 sites (as recently calculated for isolated octahedral defects in pure forsterite; Brodholt 1997). Alternatively, it may be explained by the relative sizes of the octahedral sites and cations. The average M1-O and M2-O bond lengths are 2.164 and 2.046 Å, respectively, in laihunite-3*M* (Shen et al. 1986), and 2.17 and 2.03 Å in the Mg-laihunite structure (2.20 Å in "a" sites, 2.02 Å in "b" sites, 2.17 Å in "c" sites, and 2.03 Å in "d" sites). Fe^{3+} is significantly smaller than either Fe^{2+} or Mg^{2+} (ionic radii in octahedral coordination are 0.65, 0.78, and 0.72 Å, respectively; Shannon 1976). Thus, the similar ordering behavior may simply reflect a preference for ordering with the smaller ion in the smaller octahedral site. Similarly strong preferences of Fe^{3+} for the M2 site can be predicted for laihunite-like structures produced by oxidation of FeCo, FeMn, and FeCa olivines based on octahedrally coordinated ionic radii of 0.75 Å for Co^{2+}, 1.00 Å for Ca^{2+}, and 0.83 Å for Mn^{2+} (Shannon 1976), but cannot be tested because of the lack of structure refinements for these compositions.

Fully oxidized Mg-laihunite with an Mg/(Fe+Mg) ratio of 0.5 presumably forms by an oxidation reaction such as:

$$Mg^{2+}_{1.2-x}Fe^{2+}_{0.80+x}SiO_4 + 0.8H^+ + 0.2O_2 \rightarrow \square_{0.40}Mg^{2+}_{0.80}Fe^{3+}_{0.80}SiO_4 + xFe^{2+} + (0.4 - x)Mg^{2+} + 0.4H_2O$$

where x represents the amount of Fe^{2+} being replaced by vacancies, and lies between 0 (all vacancies produced by Mg loss, implying oxidation of Fo 60) and 0.4 (all vacancies produced by Fe loss, implying oxidation of Fo 40).

Based on their interpretation of the defects in the Abert Rim specimen as intergrowths of laihunite with normal olivine, Banfield et al. (1990) suggested a formation process in which the defects served as conduits for enhanced diffusion along an oxidation front migrating inward from grain boundaries. The observation of a strong association between apparently similar defects in oxidized mantle peridotite xenoliths (specimens Ba-2-1 and DH101 from the Dish Hill cinder cone, Deadman Lake Volcanic Field, California; Banfield et al. 1992) and grain boundaries or dislocations is also consistent with formation of defects in areas with access to fast diffusion pathways, possibly assisted by strain-enhanced ordering. Although this formation mechanism cannot be eliminated based on our new results, the extensive oxidation of the olivine between the defects suggests an alternative in which defects form as a result of local ordering in a pervasively oxi-

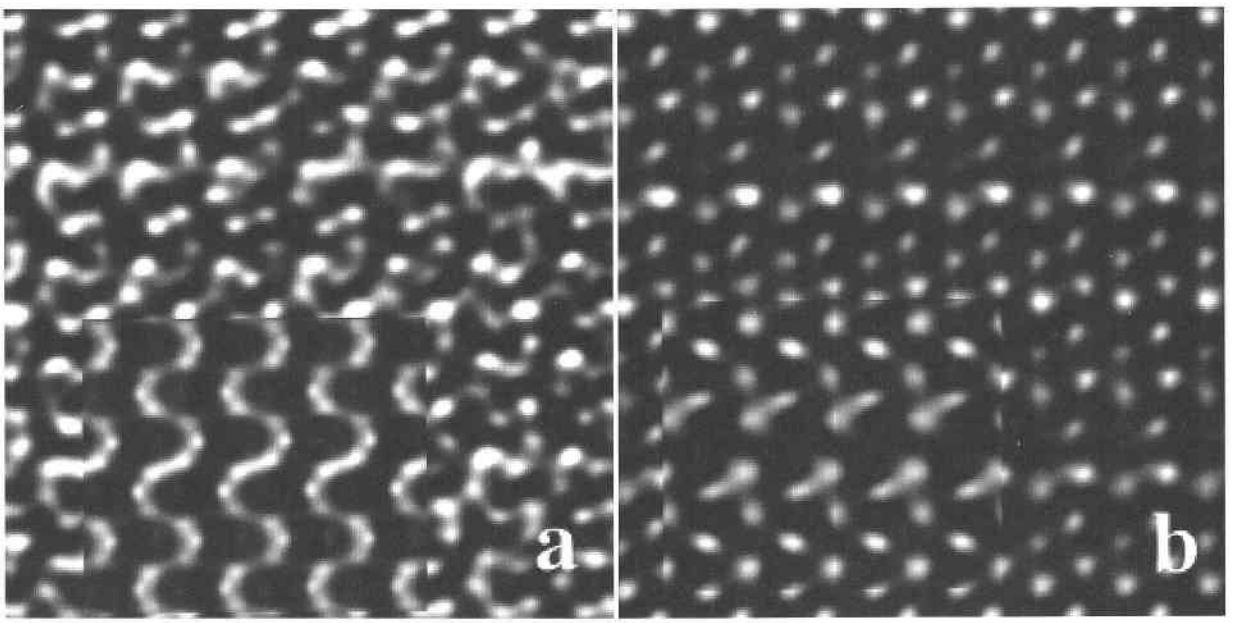

FIGURE 8. Comparison between observed and simulated images for the single-defect-row structure with $a_{ed} = 0.45$, $b_{occ} = 1$, $c_{ed} = 0.65$, $d_{occ} = 1$, and all Fe as Fe^{3+} (Table 4a). Two unit cells of the simulated structure are superimposed on each observed image. Observed images have been processed by rotational filtering using the NCEM package of Kilaas and Siddnei implemented within Digital Micrograph version 2.5 to remove noise and contributions from amorphous material; contrast has been adjusted in all images. (**a**) Scherzer defocus, 6.7 nm thickness. (**b**) ~66 nm overfocus, 15.0 nm thickness.

dized region, possibly enhanced by strain at grain boundaries and dislocations. Observations of short, uniformly distributed defects not associated with dislocations or grain boundaries in the Dish Hill specimens (Banfield et al. 1992) support this second scenario.

In summary, image simulations and observations of planar defects in an oxidized FeMg olivine at Scherzer defocus and 6.7 nm thickness are not consistent with intergrowths or precipitates of laihunite-like minerals in an olivine host (Banfield et al. 1990, 1992; Khisina et al. 1995). Instead, they appear to be integral parts of a distorted olivine structure similar to that of end-member Fe-laihunite-3*M* (Shen et al. 1986), but with only one defect row per unit cell.

Consistent trends in simulated images indicate that there must be large amounts of vacancies in M1 sites (requiring a high degree of oxidation of the Fe) and a high degree of ordering with vacancies in M1 sites, iron in M2 sites, and Mg distributed between sites of both types with a preference for M1 sites.

TEM images of areas with more widely spaced defects (e.g., parts of Fig. 1) show features similar to those in the 3-layer structures presented here. In particular, the absence of stair-step offsets in the light-colored curves suggests that the material between the defects may have an ordering scheme and level of M1 vacancies similar to those in the 3-layer spacing.

ACKNOWLEDGMENTS

Funding was provided by NSF grant EAR-9317082 to J.F.B. The authors are grateful to David J. Smith and the Center for High Resolution Electron Microscopy for the high-resolution electron micrographs and to David R. Veblen for suggestions during the early phase of this work. Reviews by Alain Baronnet, Michael Czank, and two anonymous reviewers led to significant improvements in the manuscript.

REFERENCES CITED

Banfield, J.F., Veblen, D.R., and Jones, B.F. (1990) Transmission electron microscopy of subsolidus oxidation and weathering of olivine. Contributions to Mineralogy and Petrology, 106, 110–123.

Banfield, J.F., Dyar, M.D., and McGuire, A.V. (1992) The defect microstructure of oxidized mantle olivine from Dish Hill, California. American Mineralogist, 77, 977–986.

Brodholt, J. (1997) Ab initio calculations on point defects in forsterite (Mg_2SiO_4) and implications for diffusion and creep. American Mineralogist, 82, 1049–1053.

Chakraborty, S. (1997) Rates and mechanisms of Fe-Mg interdiffusion in olivine at 980–1300°C. Journal of Geophysical Research—Solid Earth, 102, 12317–12331.

Chen, J., Li, R., Parise, J.B., and Weidner, D.J. (1996) Pressure-induced ordering in $(Ni,Mg)_2SiO_4$ olivine. American Mineralogist, 81, 1519–1522.

Doyle, P.A. and Turner, P.S. (1968) Relativistic Hartree-Fock X-ray and electron scattering factors. Acta Crystallographica, A24, 390–397.

Fujino, K., Sasaki, S., Takèuchi, Y., and Sadanaga, R. (1981) X-ray determination of electron distributions in forsterite, fayalite and tephroite. Acta Crystallographica, B37, 513–518.

Ghose, S., Wan, C., and McCallum, I.S. (1976) Fe^{2+}-Mg^{2+} order in an olivine from the lunar anorthosite 67075 and the significance of cation order in lunar and terrestrial olivines. Indian Journal of Earth Sciences, 3, 1–8.

Iishi, K., Kadomi, M., and Okamoto, K. (1989a) Synthesis of laihunite by heating Fe-Mn olivine in air. Neues Jahrbuch für Mineralogie Monatshefte, 6, 245–254.

Iishi, K., Okamoto, K., and Kadomi, M. (1989b) Formation of laihunite from Fe-(Mg, Co, Mn, Ca) olivines. Neues Jahrbuch für Mineralogie Monatshefte, 8, 345–356.

Kan, X. and Coey, J.M.D. (1985) Mössbauer spectra, magnetic and electrical properties of laihunite, a mixed valence iron olivine mineral. American Mineralogist, 70, 576–580.

Khisina, N.R., Khramov, D.A., Kolosov, M.V., Kleschev, A.A., and Taylor, L.A. (1995) Formation of ferriolivine and magnesioferrite from Mg—Fe-olivine: reactions and kinetics of oxidation. Physics and Chemistry of Minerals, 22, 241–250.

Khisina, N.R., Khramov, D.A., Kleschev, A.A., and Rusakov, V.S. (1996) Mössbauer spectroscopy data on oxidation kinetics of Mg—Fe-olivine. Physics and Chemistry of Minerals, 23, 284.

Kitamura, M., Shen, B., Banno, S., and Morimoto, N. (1984) Fine textures of laihunite, a nonstoichiometric distorted olivine-type mineral. American Mineralogist, 69, 154–160.

Kondoh, S., Kitamura, M., and Morimoto, N. (1985) Synthetic laihunite ($\square_x Fe^{2+}_{2-3x} Fe^{3+}_{2x} SiO_4$), an oxidation product of olivine. American Mineralogist, 70, 737–746.

Müller-Sommer, M., Hock, R., and Kirfel, A. (1997) Rietveld refinement study of the cation distribution in (Co,Mg)-olivine solid solution. Physics and Chemistry of Minerals, 24, 17–23.

Redfern, S.A.T., Henderson, C.M.B., Knight, K.S., and Wood, B.J. (1997) High-temperature order-disorder in $(Fe_{0.5}Mn_{0.5})_2SiO_4$ and $(Mg_{0.5}Mn_{0.5})_2SiO_4$ olivines: an *in situ* neutron diffraction study. European Journal of Mineralogy, 9, 287–300.

Schaefer, M.W. (1985) Site occupancy and two-phase character of "ferrifayalite." American Mineralogist, 70, 729–736.

Shannon, R.D. (1976) Revised effective ionic radii and systematic studies of interatomic distances in halides and chalcogenides. Acta Crystallographica, A32, 751–767.

Shen, B., Tamada, O., Kitamura, M., and Morimoto, N. (1986) Superstructure of laihunite-3*M* ($\square_{0.40}Fe^{2+}_{0.80}Fe^{3+}_{0.80}SiO_4$). American Mineralogist, 71, 1455–1460.

Stadelmann, P. (1991) Simulation of HREM images and 2D CBED patterns using EMS software package. Software manual 12M-EPFL, Lausanne, Switzerland.

Tamada, O., Shen, B., and Morimoto, N. (1983) The crystal structure of laihunite ($\square_{0.40}Fe^{2+}_{0.80}Fe^{3+}_{0.80}SiO_4$)—nonstoichiometric olivine-type mineral. Mineralogical Journal, 11, 382–391.

Manuscript received March 6, 1997
Manuscript accepted February 16, 1998
Paper handled by Charles A. Geiger

Appendix 1. Equations for local charge balance

Each M1 coordination octahedron in olivine and laihunite-like structures (including the single-defect-row structure) shares edges with two M1 and two M2 octahedra in the same zigzag, and corners with four M2 octahedra in adjacent zigzags. Similarly, each M2 coordination octahedron shares edges with two M1 octahedra in the same zigzag, and corners with four M1 and four M2 octahedra in the adjacent zigzags. All of these neighboring sites contribute to maintaining local charge balance around an octahedral site with a charge other than +2. However, only cations in octahedral sites of different types (M1 or M2) in the same zigzag are explicitly represented in the charge-balance equations because of symmetry and the assumption that the defects involve only one row of M1 sites and the two adjacent rows of M2 sites. Thus, for example, charge-balance equations for a "d" site include only the adjacent "c" sites in the same zigzag.

Equations 9 and 10 express local charge-balance requirements for "c" and "d" sites, respectively.

$$2c_1 + \text{charge}_{Fe} \times c_2 + 0.5 \times 2 \times [(2d_1 + \text{charge}_{Fe} \times d_2) - 2] = 2 \quad (9)$$

$$2d_1 + \text{charge}_{Fe} \times d_2 - 0.5 \times 2 \times [2 - (2c_1 + \text{charge}_{Fe} \times c_2)] = 2 \quad (10)$$

The total charge from the cations in each "c" site is $2c_1 + \text{charge}_{Fe} \times c_2$, so that $2 - (2c_1 + \text{charge}_{Fe} \times c_2)$ is the charge deficiency in the site. Similarly, the total charge from the cations in each "d" site is $2d_1 + \text{charge}_{Fe} \times d_2$, and $(2d_1 + \text{charge}_{Fe} \times d_2) - 2$ is the excess charge in the site. Each "c" site receives half of the excess charge from each of two adjacent "d" sites, and each "d" site compensates for half of the charge deficiency in each of the two adjacent "c" sites.

Equation 5 results from algebraic simplification of Equations 9 and 10.

Equation 11 expresses the local charge-balance requirements for a "b" site.

$$2b_1 + \text{charge}_{Fe} \times b_2 - 0.5 \times [2 - (2c_1 + \text{charge}_{Fe} \times c_2)] - 0.5 \times (2 - 2a_1) = 2 \quad (11)$$

It says that the total charge in a "b" site ($2b_1 + \text{charge}_{Fe} \times b_2$) satisfies half the charge deficiency in a "c" site $\{0.5 - [2 - (2c_1 + \text{charge}_{Fe} - c_2)]\}$ and half the charge deficiency in an "a" site $[0.5 \times (2 - 2a_1)]$, with the average octahedral charge (2) left over.

Equation 12 expresses the local charge-balance requirements for an "a" site.

$$2a_1 + 2 \times \{(2b_1 + \text{charge}_{Fe} \times b_2) - 2 - 0.5 \times [2 - (2c_1 + \text{charge}_{Fe} \times c_2)]\} = 2 \quad (12)$$

It says that each of two "b" sites gives the "a" site the excess charge $[(2b_1 + \text{charge}_{Fe} \times b_2) - 2]$ that is left over after compensating for half of the charge deficiency in the "c" site on its other side $\{0.5 \times [2 - (2c_1 + \text{charge}_{Fe} \times c_2)]\}$.

When both sides of Equation 11 are multiplied by 2, it and Equation 12 both simplify to produce Equation 6.